TUDelft

Delft University of Technology

Giant anisotropic magnetocaloric effect by coherent orientation of crystallographic texture and rare-earth ion moments in HoNiSi ploycrystal

Zhang, Hu; Xing, Chengfen; Zhou, He; Zheng, Xinqi; Miao, Xuefei; He, Lunhua; Chen, Jie; van Eijk, Lambert; Brück, Ekkes; More Authors

Important note
To cite this publication, please use the final published version (if applicable).
Please check the document version above.

Full length article

Giant anisotropic magnetocaloric effect by coherent orientation of crystallographic texture and rare-earth ion moments in HoNiSi ploycrystal

Hu Zhang[a,*], Chengfen Xing[a], He Zhou[a], Xinqi Zheng[a], Xuefei Miao[b], Lunhua He[c,d,e], Jie Chen[e],
Huaile Lu[e,f], Enke Liu[c], Wentuo Han[a], Hongguo Zhang[g], Yixu Wang[a], Yi Long[a],
Lambert van Eijk[h], Ekkes Brück[h]

[a] School of Materials Science and Engineering, University of Science and Technology of Beijing, Beijing 100083, PR China
[b] School of Materials Science and Engineering, Nanjing University of Science and Technology, Nanjing 210094, PR China
[c] State Key Laboratory for Magnetism, Beijing National Laboratory for Condensed Matter Physics, Institute of Physics, Chinese Academy of Sciences, Beijing 100190,
PR China
[d] Songshan Lake Materials Laboratory, Dongguan 523808, PR China
[e] Spallation Neutron Source Science Center, Dongguan 523803, PR China
[f] Beijing Advanced Innovation Center for Materials Genome Engineering, State Key Laboratory for Advanced Metals and Materials, University of Science and Tech-
nology Beijing, Beijing 100083, P R China
[g] School of Materials Science and Engineering, Beijing University of Technology, Beijing 100124, P R China
[h] Fundamental Aspects of Materials and Energy, RST, Delft University of Technology, Mekelweg 15, 2629 JB Delft, the Netherlands

ARTICLE INFO

ABSTRACT

A new concept named "rotating magnetocaloric effect (RMCE)" has been proposed and attracted more atten-
tion recently. Unlike the traditional MCE that is achieved by moving the magnetic refrigerant in and out of
magnetic field, RMCE can be realized by rotating the anisotropic material within the static field, thus imply-
ing the possible higher efficiency and simpler device. However, most studies on RMCE are concentrated on
single crystals, which are generally more expensive and difficult to prepare in comparison with polycrystals.
Therefore, it is highly desirable to search polycrystalline materials with high RMCE. Here, the textured HoNiSi
polycrystal is reported to show a giant RMCE, e.g., the rotating magnetic entropy change ($-\Delta S_R$) are 18.5 and
26.7 J/kg K and rotating adiabatic temperature change (ΔT_R) are 7.0 and 13.4 K under 2 and 5 T, respectively.
This giant RMCE over a wide temperature range especially under low field suggests textured HoNiSi as prom-
ising material for practical application of rotary magnetic refrigeration. Moreover, the large magnetic anisot-
ropy of HoNiSi is explained by the single-ion magnetic anisotropy theory, and the coherent orientation of
crystallographic texture and rare-earth ion moments leads to the large RMCE in the textured HoNiSi
polycrystal. This work reveals that the strongly coherent orientation of crystallographic texture and rare-
earth ion moments is a key to realize large RMCE in polycrystalline materials.

© 2020 Acta Materialia Inc. Published by Elsevier Ltd. All rights reserved.

1. Introduction

Cooling technology plays an increasingly important role in our
modern society covering a wide range of aspects from industrial gas
liquefaction and scientific research to domestic air conditioning and
refrigerator. At present, the predominant gas compression-expansion
refrigerator units can only attain 40% of ideal Carnot efficiency, and it
has a small potential to further improve the efficiency largely [1,2]. In
addition, the traditional cooling technique usually use some harmful
refrigerants such as chlorofluorocarbons (ozone-depleting chemicals)

and hydrofluorocarbons (greenhouse gases), which have a negative
impact on the environment [3]. Therefore, searching new refrigera-
tion technology with high energy efficiency and environmental
friendly is very urgent.

In recent years, magnetic refrigeration based on magnetocaloric
effect (MCE) has been developed as a promising cooling technology
due to its higher energy efficiency and lower environmental impact
than the conventional gas compression refrigeration [4,5]. Since the
discovery of giant MCE in $Gd_5(Si, Ge)_4$, room temperature magnetic
refrigeration has attracted much attention, and a series of magnetic
materials have been reported to exhibit large MCE around room tem-
perature [6–10]. In addition to the room temperature magnetic
refrigeration, the research on low temperature magnetic refrigeration

is also important due to its potential utilization in gas liquefaction and scientific research [11−13]. Moreover, since the maximum field supplied by permanent magnet is usually lower than 2 T, it is desirable to search materials with large MCE especially under low magnetic field.

In the past decades, numerous studies have been focused on the MCE related to the change of exchange energy during the magnetic phase transition [3,14,15]. In contrast, little interests have been paid to the MCE contributed by the change of magnetic anisotropy energy because it was believed to be much lower than the contribution from magnetic exchange energy [16]. However, recent studies reveal that the contribution from magnetic anisotropy energy could also be remarkable during the rotation of spontaneous magnetization vector [16,17]. Based on this fact, a new concept named "rotating magnetocaloric effect (RMCE)" has been proposed. Unlike the conventional MCE that needs to be realized by moving material in and out of magnetic field, the RMCE can be fulfilled by simply rotating the material in a constant field, suggesting the possible higher efficiency and simpler device [17]. Thus, it opens a new research field of MCE and attracts more and more attention.

Due to the high magnetic moments and low ordering temperature of rare earth elements, many rare earth-based materials have been found to exhibit large MCE at low temperatures [11,12,18]. In addition, rare earth-based materials often show strong magnetic anisotropy, thus making them good candidates for RMCE materials at low temperatures. So far, some rare earth-based single crystals have been reported to present large RMCE [16,19,20]. However, high cost and complex preparation is a serious issue for the commercial application of single crystals, and so it is highly preferable to explore the large RMCE in polycrystalline materials.

In our previous work, a giant RMCE was first found in the textured polycrystalline DyNiSi, proving the possible to obtain large RMCE in polycrystals [21]. However, in some materials with canted magnetic structure, a large RMCE may not be obtained by the rotation of textured polycrystal since the alignment of magnetic moments deviates from the crystallographic orientation [22]. In this context, we believe that the coherent preferred orientation of crystallographic texture and rare-earth ion moments is the key to obtain the large RMCE in polycrystalline materials. In present work, we found that the textured HoNiSi polycrystal shows a strongly coherent orientation of crystallographic texture and rare-earth Ho^{3+} ion moments, which then leads to a giant RMCE. This work not only demonstrates our point of view, but also reports a new material with the highest RMCE so far.

2. Experimental

Sample synthesis: The polycrystalline HoNiSi compound was synthesized by arc-melting appropriate proportion of constituent components with the purity better than 99.9 wt.% in a water-cooled copper hearth under purified argon atmosphere. As shown in Fig. 1 (a), the top of sample was melted by electric arc and the temperature could reach over 3500 °C, while the bottom of sample was cooled by circulating water, causing a large temperature gradient between the bottom and top of the sample. Thus, the texture structure with a series of columnar grains grows along the direction of solidification with a high cooling rate ($\sim 10^2$ K s^{-1} [23,24]). The as-cast sample was wrapped in tantalum foil and annealed in a high-vacuum quartz tube at 1073 K for a week followed by liquid nitrogen quenching.

Crystal structure characterization: The room-temperature powder X-ray diffraction (XRD) measurement was performed using Cu $K\alpha$ radiation, and then the Rietveld refinement based on the XRD pattern was carried out to identify the crystal structure using LHPM Rietica software [25]. In order to investigate the texture structure, the XRD pattern of bulk sample was taken on the surface of sample which is perpendicular to the orientation of columnar grains as shown in Fig. 2(a). The grain orientation and morphology were investigated by

the electron backscatter diffraction (EBSD) using a field emission scanning electron microscope (FE-SEM).

Neutron powder diffraction (NPD) experiments: NPD experiments measured at different temperatures ranging from 2 to 20 K are performed on the general purpose powder diffractometer (GPPD) at the China Spallation Neutron Source (CSNS) in Dongguan, China. Samples are loaded in 9.1 mm vanadium cans and diffraction patterns are collected in the time-of-fight (T. O. F.) mode with wavelength bands of $0.1 − 4.9$ Å. The program of FullProf was used for the Rietveld refinement of crystal structures and magnetic structures.

Physical property measurements: The alternating current (AC) susceptibilities in zero direct current (DC) field and specific heat capacities along different directions under different magnetic fields were measured by using a physical property measurement system (PPMS) from Quantum Design Inc. For magnetic measurements, a rectangular-like sample of 4.77 mg ($2 \times 0.9 \times 0.9$ mm^3) as shown in Fig. 1(a) was sliced from the annealed ingot with the major axis along the longitudinal direction of columnar grains. Magnetization was measured using a superconducting quantum interference device (SQUID) magnetometer from Quantum Design Inc (model MPMS-XL). The sample was measured with the major axis being parallel and perpendicular to the magnetic field, respectively. The demagnetization correction was carried out to eliminate the influence of demagnetizing field. Assuming that the effective field in the material is homogeneous, the average effective field H_{int} can be estimated by subtracting the demagnetization field $H_d = N_d M$ from the external field H_{ext},

$$\text{Hint} = \text{Hext} - \text{NdM} \tag{1}$$

where N_d is the demagnetization factor and is calculated to be 0.1867 and 0.4116 along parallel and perpendicular directions, respectively [26]. All the discussions hereafter are based on the data after the demagnetization correction.

Electron Localization Function (ELF) calculations: The Electron Localization Function (ELF) of HoNiSi compound was calculated using the Stuttgart TB-LMTO-ASA code (version 4.7). Tetrahedron method was employed to treat the first Brillion zone. A $20 \times 33 \times 19$ k-mesh sampling was used from the initial self-consistent-field calculations to the final ELF calculations. Two additional kinds of empty spheres were added to achieve 100% cell volume within the overlapping limits. The overall overlapping volume is 7.594%. Convergence problems stemming from the highly localized $4f$ electrons of Ho atoms were solved by down folding the $4f$ electrons into the core region [27].

3. Results

3.1. Highly preferred crystallographic orientation

Fig. 1(b) shows the powder XRD pattern of HoNiSi compound measured at ambient temperature and Rietveld refinement to the experimental data. The Rietveld refinement of powder XRD pattern confirms that the sample crystallizes in a single phase with the TiNiSi-type orthorhombic structure (space group *Pnma*). The lattice parameters at room temperature determined from Rietveld refinement are a = 8.828(6) Å, b = 4.149(2) Å, and c = 7.168(1) Å, which are in a good agreement with the data in previous reports [28,29]. Fig. 2 (a) shows both the powder and bulk XRD patterns. In comparison with powder XRD pattern which shows a random crystallographic orientation, it is clearly seen that many diffraction peaks are suppressed while a few peaks become higher in the bulk XRD pattern, revealing the presence of highly preferred crystallographic orientation. Moreover, the (020) diffraction peak increases significantly, suggesting that the columnar grains are aligned with the <010> preferred orientation.

In order to further investigate the crystallographic orientation, the EBSD orientation map of the cross section perpendicular to the longitudinal direction of columnar grains with Z_0 parallel to the
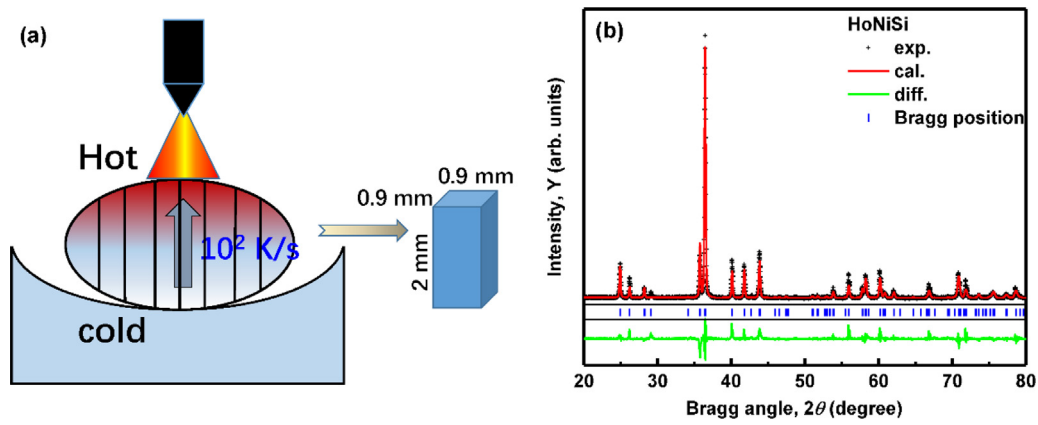
Fig. 1. (a) Schematic of the preparation of the textured HoNiSi polycrystal. (b) The observed (cross point) and calculated intensities (line drawn through the data points) of powder XRD patterns of HoNiSi compound at room temperature. The short vertical lines indicate the Bragg peak positions of TiNiSi-type orthorhombic structure. The lower curve shows the difference between the observed and calculated intensities.

solidification direction (SD) was measured as shown in Fig. 2(b). It is found that the alloy presents a strong texture structure with the <010> preferred orientation parallel to the SD, consistent with the result from XRD measurement. Fig. 2(c) displays the inverse pole figures along X_0, Y_0, and Z_0 (SD) axes determined from EBSD measurements. It further confirms that the HoNiSi compound not only develops a strong <010> preferred orientation parallel to the SD, but also shows the highly preferred orientations <001> and <100> along the other two directions X_0 and Y_0, respectively. This strong preferred orientation of HoNiSi is beneficial for attaining large magnetic anisotropy as well as RMCE.

3.2. Neutron powder diffraction (NPD) study

High resolution neutron powder diffraction (NPD) was carried out at different temperatures to investigate the magnetic structure of HoNiSi. Fig. 3(a) shows the NPD pattern at 2 K and the Rietveld

refinement of the experimental data. No ordered magnetic moment can be obtained on Ni atoms from the refinement and the magnetic moment of Ho is determined to be 7.07 (2) μ_B, suggesting that the magnetic moment of HoNiSi is completely contributed by Ho atoms. Moreover, the Ho magnetic moments align along the b-axis and form an antiferromagnetic (AFM) structure with a wave propagation vector $k = [0.5, 0.0, 0.5]$ as shown in Fig. 3(b). It indicates that the b-axis is the easy magnetization axis, in a good agreement with the previous NPD study [28]. Besides, this easy magnetization axis is consistent with the preferred crystallographic orientation, suggesting the strongly coherent preferred orientation of crystallographic texture and rare-earth ion moments.

Figs. 4(a) shows the NPD pattern at 5 K and Rietveld refinement to the experimental data. The refinement reveals that no ordered magnetic structure is identified at 5 K, indicating that the HoNiSi exhibits the paramagnetic (PM) state. Furthermore, Fig. 4(b) shows the NPD patterns at different temperatures ranging from 2 K to 20 K. No
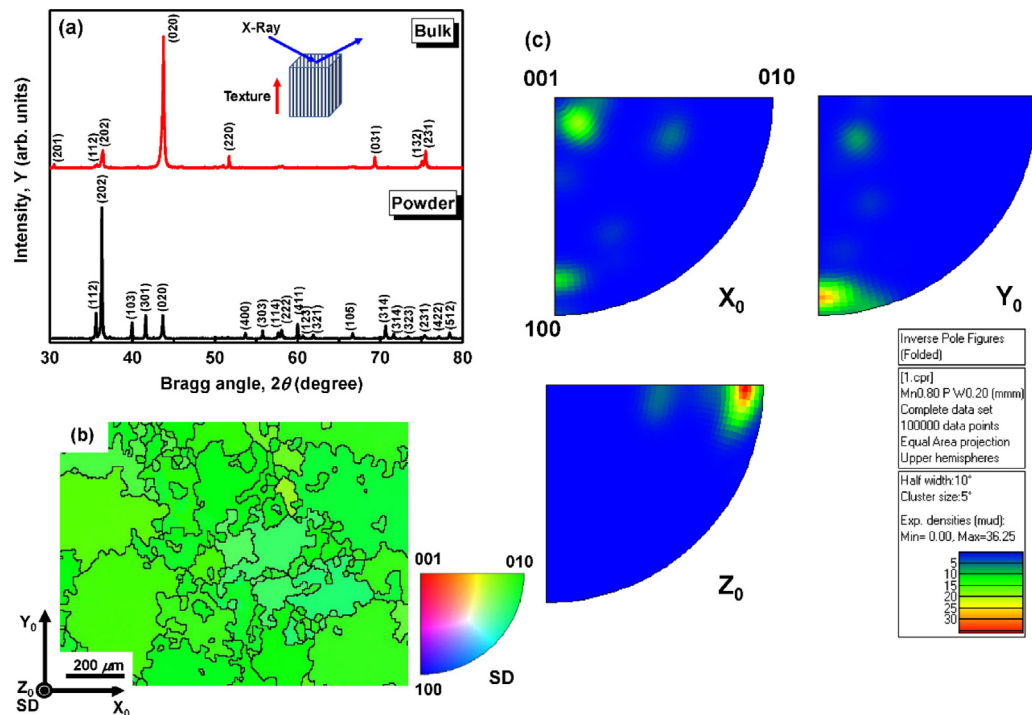

Fig. 2. (a) XRD patterns carried out on HoNiSi powder and on the bulk surface perpendicular to the longitudinal direction of columnar grains at room temperature. (b) EBSD orientation map [inverse pole figure (IPF) mode] of the cross section perpendicular to the longitudinal direction of columnar grains with Z_0 parallel to the solidification direction (SD). (c) The inverse pole figures along X_0, Y_0, and Z_0 (SD) axes determined from EBSD measurements.
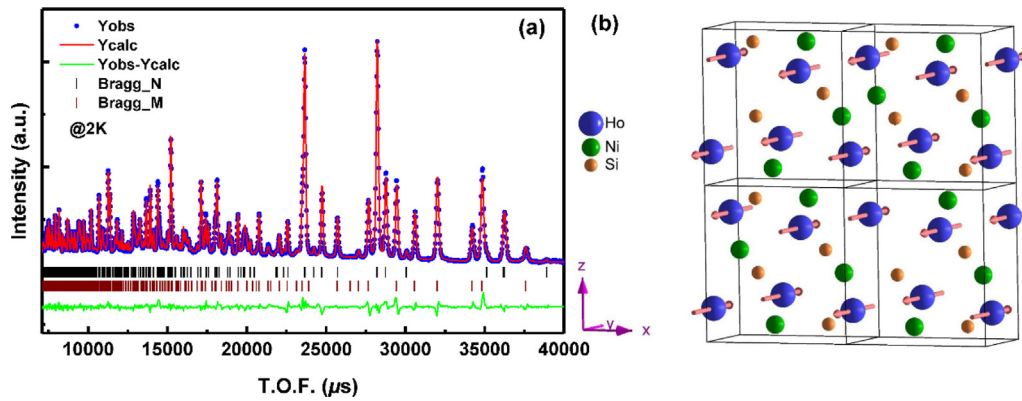
Fig. 3. (a) NPD pattern of HoNiSi compound at 2 K and Rietveld refinement to the experimental data. (b) Schematic of magnetic structure at 2 K indicating the antiferromagnetic structure.

obvious difference of NPD patterns can be found above the Néel temperature (T_N) of 3.8 K in the temperature range of $5 - 20$ K, proving that HoNiSi shows a predominant PM state and does not exhibit a magnetic phase transition in this temperature range. Fig. 4(c) shows the temperature dependence of Ho moment. It is found that the magnetic moment of Ho decreases sharply from 7.07 μ_B to nearly 0 around T_N, corresponding to the AFM-PM transition. No ordered magnetic moment can be obtained above T_N, proving the predominant PM state.

3.3. Strong anisotropy of magnetic properties

Figs. 5(a) and (b) display the specific heat (C_P) for HoNiSi under the different fields with the magnetic field parallel and perpendicular to the texture orientation, respectively. Both C_P curves show a peak at 3.5 K under zero field, corresponding to the AFM-PM transition. Besides, a broad bump is observed around T_1. Considering that no ordered magnetic structure is detected from NPD above T_N, we speculate that this bump is likely related to the presence of short-range ordering in PM state [29]. With the application of magnetic field along the parallel direction, the T_N peak is depressed and merges with the bump, and shifts to higher temperature with increasing field. It reveals that the AFM state is induced into the ferromagnetic

(FM) state by applying the magnetic field. In contrast, the T_N peak is hard to be depressed even under 2 T along the perpendicular direction, and both T_N and T_1 do not move with increasing field. This fact suggests that the AFM coupling is hard to be induced into the FM coupling when the field is perpendicular to the easy magnetization axis. This result is also confirmed by the analysis of *M-T* curves under various magnetic fields as shown in Fig. 6.

Figs. 6(a) and (b) show the temperature dependence of zero-field-cooling (ZFC) and field-cooling (FC) magnetization under 0.05 T with the magnetic field along the parallel and perpendicular directions, respectively. The magnetization along parallel direction is nearly one order of magnitude higher than that along the perpendicular direction, suggesting the strong magnetocrystalline anisotropy (MCA). The T_N peak is observed at 3.8 K along both directions, corresponding to the AFM-PM transition. Interestingly, two bumps around T_1 and T_2 are observed above T_N and a distinct discrepancy between ZFC and FC curves appears below T_2 along the perpendicular direction. These phenomena have not been found in *M-T* curves along the parallel direction. It is well known that the thermomagnetic irreversibility between the ZFC and FC curves is generally observed in spin glass systems [30] or magnetic materials with narrow domain walls [18,31]. Fig. 6(c) shows the temperature dependence of AC magnetic susceptibility (χ') of HoNiSi at different frequencies ranging from 10
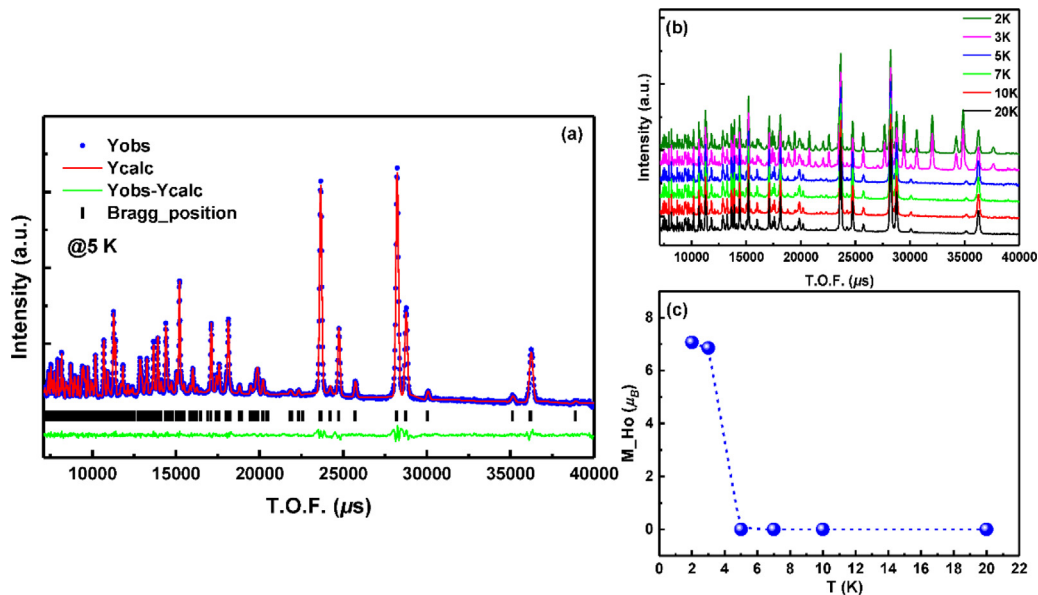

Fig. 4. (a) NPD pattern of HoNiSi compound at 5 K and Rietveld refinement to the experimental data. (b) NPD patterns above T_N ranging from 2 to 20 K. (c) The temperature dependence of Ho moment determined from the Rietveld refinement of NPD data.
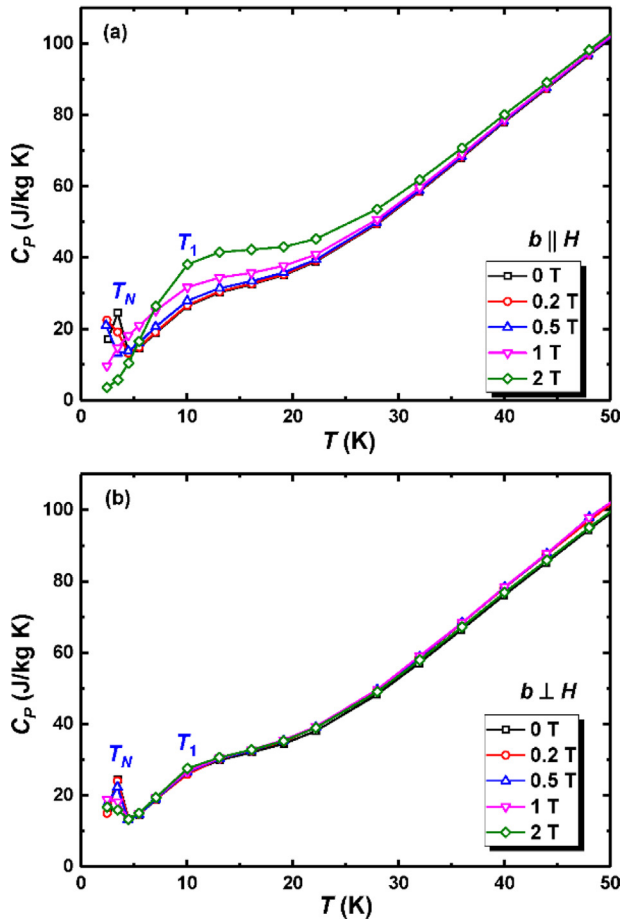
Fig. 5. Specific heat (C_P) for HoNiSi under different fields with the magnetic field (a) parallel and (b) perpendicular to the texture orientation, respectively.

to 9997 Hz. In addition to the peak at T_N, a slight bump is found around T_1 and no anomaly can be seen around T_2. Moreover, the T_1 peak position does not shift with the variation of frequency, suggesting that the thermomagnetic irreversibility is not related to the spin glass. Considering the very low ordering temperature and considerably large MCA, the domain wall width of HoNiSi would be comparable to that of the lattice spacing, thus leading to the narrow domain wall pinning effect [18,32]. Therefore, the bumps around T_1 and T_2 as well as the thermomagnetic irreversibility along perpendicular direction are likely related to the narrow domain wall pinning effect. As sketched in Fig. 6(b), in ZFC mode, the domain walls are pinned along the easy magnetization axis and hard to be magnetized by the perpendicular magnetic field, which leads to the low magnetization at low temperatures. With the increase of temperature, thermal energy becomes strong enough to overcome the energy barriers presented by the pinning centers, thus resulting in the presence of short-range FM ordering that leads to the increase of magnetization just above T_N. With further increasing temperature, the magnetic ordering is destructed by thermal disturbance, causing the decrease of magnetization above T_1. These competitive effects between the thermal activation and thermal disturbance on magnetization give rise to the bumps around T_1 and T_2. In contrast, in FC mode, the magnetic field is applied at high temperature and so magnetic moments are hardly pinned and move in the direction of magnetic field during cooling. Therefore, the magnetization in FC mode is higher than that in ZFC mode. On the other hand, when the magnetic field is applied parallel to the texture orientation, narrow domain wall pinning effect disappears since the easy magnetization axis is consistent with direction

of magnetic field, and so the bumps and the thermomagnetic irreversibility are not observed.

Fig. 6(d) shows the temperature dependence of inverse DC susceptibility (χ^{-1}) fitted to the Curie-Weiss law in the field of 1 T along parallel and perpendicular directions, respectively. Both χ^{-1} curves along different directions obey the Curie-Weiss law in PM region. Based on the Curie-Weiss fitting, the effective magnetic moment (μ_{eff}) is determined to be 10.49 μ_B and 10.76 μ_B along parallel and perpendicular directions, respectively, which are close to the theoretical magnetic moment (10.60 μ_B) of Ho^{3+} free ion, implying the absence of localized magnetic moment on Ni atoms. The PM Curie temperature (θ_p) is 8.9 K and −6.5 K, along the parallel and perpendicular directions, respectively. The negative θ_p indicates the predominant AFM interaction along the perpendicular direction, while the positive θ_p implies that the AFM state is unstable and can be induced into FM state along the parallel direction. Another feature worth noticing is that both χ^{-1} curves do not follow the Curie-Weiss law below ∼20 K. This deviation from the Curie-Weiss law at temperatures just above T_N is generally attributed to the presence of short-range FM correlations [31,33], further confirming our above speculation.

Fig. 6(e) and 6(f) shows the *M-T* curves under various magnetic fields along the parallel and perpendicular directions, respectively. The magnetization increases largely with increasing magnetic field along the parallel direction, and the AFM state is induced into the FM state when field is higher than 0.3 T. Then the transition temperature shifts towards higher temperature with further increasing field, corresponding to the typical characteristic of FM-PM transition [29]. On the contrary, the AFM-PM transition at T_N and the slight bump around T_1 do not move and still can be seen clearly under 5 T along the perpendicular direction. This result indicates that the AFM state along perpendicular direction is too strong to be induced into the FM state, consistent with the analysis of specific heat measurements.

3.4. Large RMCE

Fig. 7(a-d) shows the magnetization isotherms along different directions. Below T_N, a field-induced metamagnetic transition from AFM to FM state is observed under the critical field of 0.23 T along the parallel direction, suggesting that the AFM coupling is unstable and easy to be induced into FM state under low field along the easy magnetization axis. The isotherms just above T_N exhibit FM behavior and even show strong curvatures up to 20 K. This result further proves the presence of short-range FM correlations in PM state [12,31]. On the other hand, the magnetization isotherms show a typical AFM behavior along the perpendicular direction, and only a slight inflection of isotherm at 2 K is seen under 1.3 T. It reveals a strong AFM coupling along the perpendicular direction that is hard to be induced into the FM state. In addition, the magnetization along the parallel direction is much higher than that along the perpendicular direction, and it changes largely with the variation of temperature along the parallel direction while the magnetization decreases slowly with increasing temperature along the perpendicular direction. This fact implies the possible high MCE along the parallel direction as well as low MCE along the perpendicular direction [18].

The entropy change (ΔS) was calculated from the magnetization isotherms using Maxwell relation $\Delta S = \mu_0 \int_0^H (\partial M / \partial T)_H dH$ [15], and Fig. 7(e) and 7(f) shows the temperature dependence of ΔS along different directions. The textured HoNiSi shows a large ΔS along parallel direction, e.g., the maximum $-\Delta S$ values is 28.4 J/kg K for a field changes of 5 T. Especially, a high $-\Delta S$ of 19.0 J/kg K is obtained under relatively low field change of 2 T. This large MCE especially under low field originates from the field-induced metamagnetic transition from weak AFM to FM state, and it is favorable to practical magnetic refrigeration using permanent magnet [29]. Besides, the ΔS peak broadens asymmetrically towards higher temperatures with the
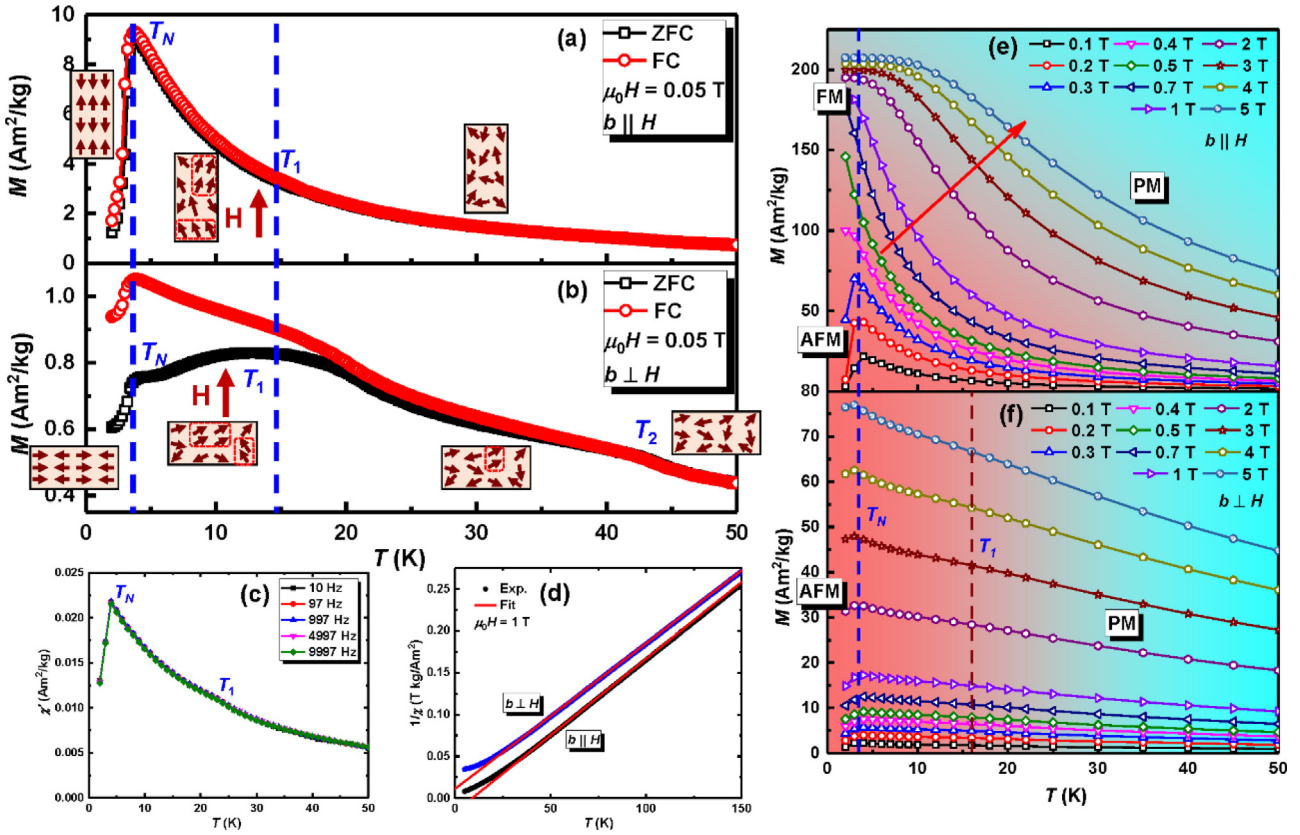
Fig. 6. Temperature dependence of zero-field-cooling (ZFC) and field-cooling (FC) magnetization under 0.05 T with the magnetic field along the (a) parallel and (b) perpendicular directions, respectively. The inserted schematic shows the ordering of magnetic moments with varying the temperature. (c) Temperature dependence of AC magnetic susceptibility (χ') of HoNiSi at different frequencies ranging from 10 to 9997 Hz. (d) Temperature dependence of inverse DC susceptibility (χ^{-1}) fitted to the Curie-Weiss law in the field of 1 T along the parallel and perpendicular directions, respectively. The M-T curves under various magnetic fields along the (e) parallel and (f) perpendicular directions, respectively.

increase of field, proving again the presence of field-induced FM correlation in PM region [31,34]. On the contrary, the ΔS along perpendicular direction is much smaller than that along the parallel direction. A negative $-\Delta S$ value (inverse MCE) is observed below T_N even under the highest field of 5 T, which is attributed to the strong AFM coupling. A slight bump appears above T_N, corresponding to the presence of field-induced trivial FM interactions around T_1. Moreover, the ΔS peak at T_N does not shift with increasing magnetic field due to the characteristic of hard magnetization axis. This large anisotropic MCE implies the possible giant rotating MCE in the textured HoNiSi compound. In addition, it is found that the $-\Delta S$ of 26.0 J/kg K under 5 T for the non-textured HoNiSi is smaller than that along the parallel direction but larger than the one along the perpendicular direction of present textured HoNiSi [29]. This fact further proves that the consistence of crystallographic texture and easy magnetization axis plays the key role to determine the large MCE.

The rotating magnetic entropy change (ΔS_R) has been calculated using the following equation [16]:

$$\Delta S_R = -\left[\left(\frac{\delta E_{a,\mu_0 H}}{\delta T}\right) - \left(\frac{\delta E_{a,0}}{\delta T}\right)\right] = -\left(\frac{\delta \Delta E_a}{\delta T}\right) \tag{2}$$

Where $E_{a,\mu_0 H}$ and $E_{a,0}$ are magnetocrystalline anisotropy energy under a magnetic field $\mu_0 H$ and zero field. Fig. 8(a) shows the M-H curves at 4 K along parallel and perpendicular directions to illustrate the calculation of magnetocrystalline anisotropy energy E_a. The E_a can be estimated by integrating the area of the M-H curves at each temperature between different directions. The E_a at 4 K as shaded area is large due to the strong MCA of textured HoNiSi. Fig. 8(b) displays the field dependence of E_a at different temperatures. The E_a decreases with increasing temperature due to the weakening of MCA caused by the thermal disturbance [35]. But the E_a still remains high

in a wide temperature above T_N. The existence of high E_a above T_N might be related to the MCA of short-range ordering and paramagnetic susceptibilities [36]. Fig. 9(a) displays the ΔS_R between the parallel and perpendicular directions as a function of temperature and magnetic field. The maximum $-\Delta S_R$ reaches as high as 18.5 and 26.7 J/kg K under 2 and 5 T, respectively. To our knowledge, this is the largest rotating ΔS_R reported so far. As another important criterion to evaluate the MCE, the rotating adiabatic temperature change (ΔT_R) can be estimated using the following equation [19]:

$$\Delta T_R = -\frac{T}{C_P(T, H_0)}\Delta S_R \tag{3}$$

Where $C_P(T, H_0)$ is zero-field heat capacity as shown in Fig. 5. Fig. 9(b) shows the ΔT_R as a function of temperature and magnetic field. Large ΔT_R of 7.0 and 13.4 K can be obtained by rotating the textured HoNiSi from perpendicular to parallel direction under a constant field of 2 and 5 T, respectively.

4. Discussion

The origin of large RMCE in the textured HoNiSi polycrystal is discussed in this section. Based on the results of NPD study and Curie-Weiss fitting, the magnetic moment of HoNiSi is contributed by Ho element, and so the magnetic anisotropy originates solely from Ho^{3+} ions. As is well known, the magnetic moment of rare earth ion is contributed by the electrons of incompletely filled 4f shell, which are strongly bound around the nucleus and shielded by the outer electrons of 5p and 6 s shells. Thus, it is reasonable to explain the magnetic anisotropy of HoNiSi by the single-ion magnetic anisotropy theory, which is predominant in magnetic materials with such localized moments [37,38]. Fig. 10(a) depicts the distribution of ELF values
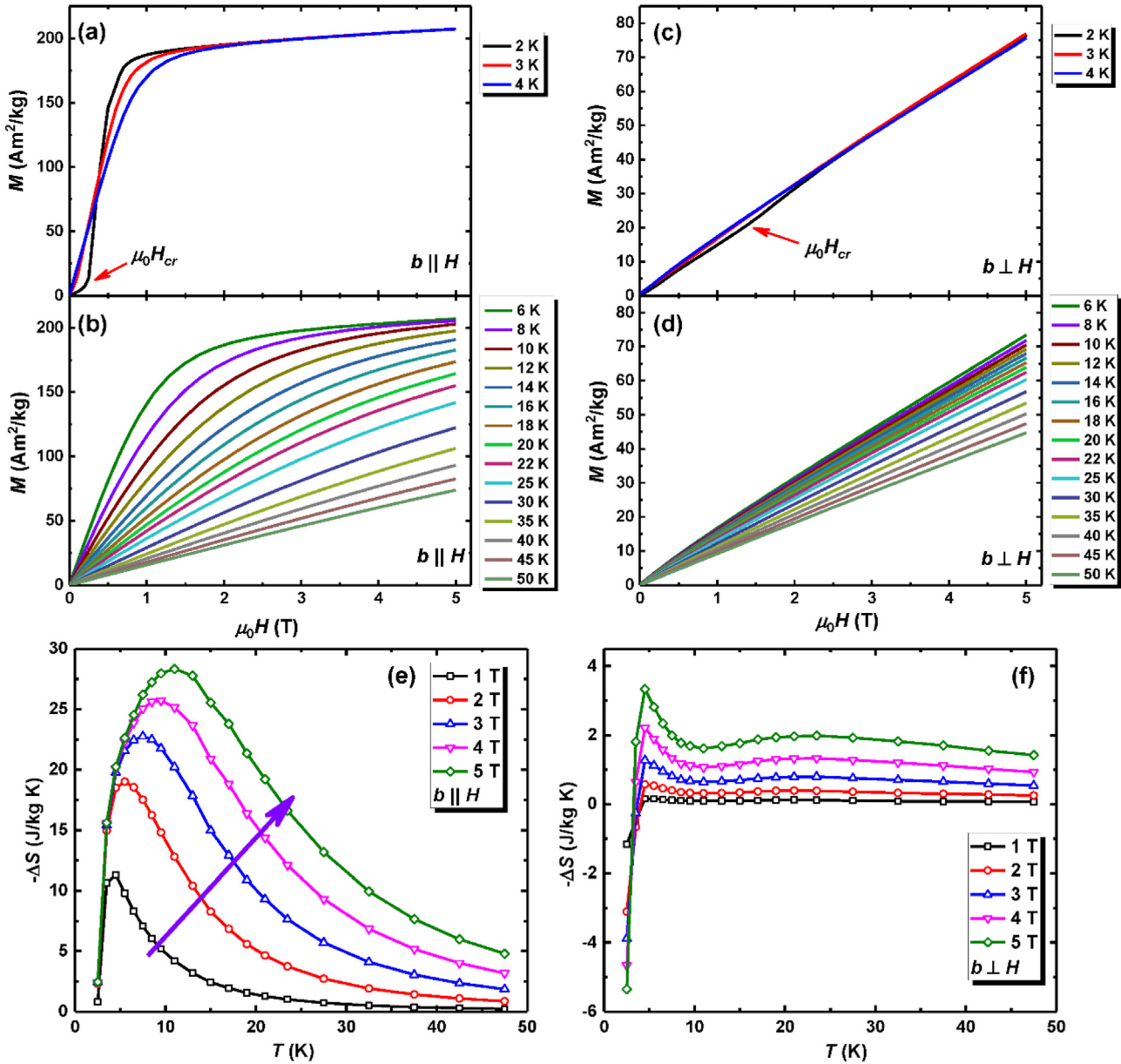
Fig. 7. Magnetization isotherms (a) below and (b) above T_N along the parallel direction as well as magnetization isotherms (c) below and (d) above T_N along the perpendicular direction. Temperature dependence of ΔS along the (e) parallel and (f) perpendicular directions, respectively.

within the 3D unit cell space. The high electron localizing and delocalizing regions are surrounding Si and Ni atoms, respectively, suggesting that the Si atoms exhibit a distinct anionic feature while the Ni atoms show the cationic characteristic. Thus, chemical bonds form between the Ni and Si atoms. The ELF distribution around Ho atoms indicaties the cationic nature of Ho ions, and no evident interaction has been found between the Ho and Ni/Si atoms. Therefore, it confirms that the magnetic behavior of HoNiSi could be interpreted by the single-ion magnetic anisotropy theory. Fig. 10(b) shows the perspective view of the TiNiSi-type crystal strucure of HoNiSi. Each Ho^{3+} ion is situated in a tetrahedral structure formed by three neighboring Ni^{1+} ions and one neighboring Si^{4-} ion. Therefore, the electronic charge cloud of Ho^{3+} ion will be affected by the crystalline electric field (CEF) caused by the neighboring Ni^{1+} and Si^{4-} ions. Since the CEF of this tetrahedral structure is non-spherical symmetrical, the electrostatic potential energy E_i of a single Ho^{3+} ion will be different when the electronic charge cloud has different angles with respect to the CEF. Thus, the E_i is minimized only when the electronic charge

cloud orients a particular direction, implying the preferred orientation. Furthermore, the spins of Ho^{3+} ion will also show preferred orientation with respect to the crystallographic axis (i.e., b-axis in this case) due to the spin-orbit coupling, leading to the MCA of HoNiSi. More importantly, this preferred orientation of Ho^{3+} ion moment is coherent with the preferred crystallographic orientation of textured HoNiSi polycrystal, thus resulting in the large MCA and RMCE of textured HoNiSi compound.

The coherence of preferred crystallographic orientation and moment orientation of Ho^{3+} ion also enables us to further investigate the RMCE of HoNiSi theoretically using the coherent rotational (CR) model [19,39]. The energy of the system can be written as [39]:

$$E = E_K + E_H = K_1 \sin^2\alpha + K_2 \sin^4\alpha - M_S H \cos(\theta - \alpha) \qquad (4)$$

Where E_K is the theoretical MCA energy, E_H is the magnetostatic energy, K_1 and K_2 are the second- and fourth-order MCA constants, M_S is the saturation magnetization that can be obtained by extrapolating $1/H$ to 0 using the M-H curve at 2 K along the easy
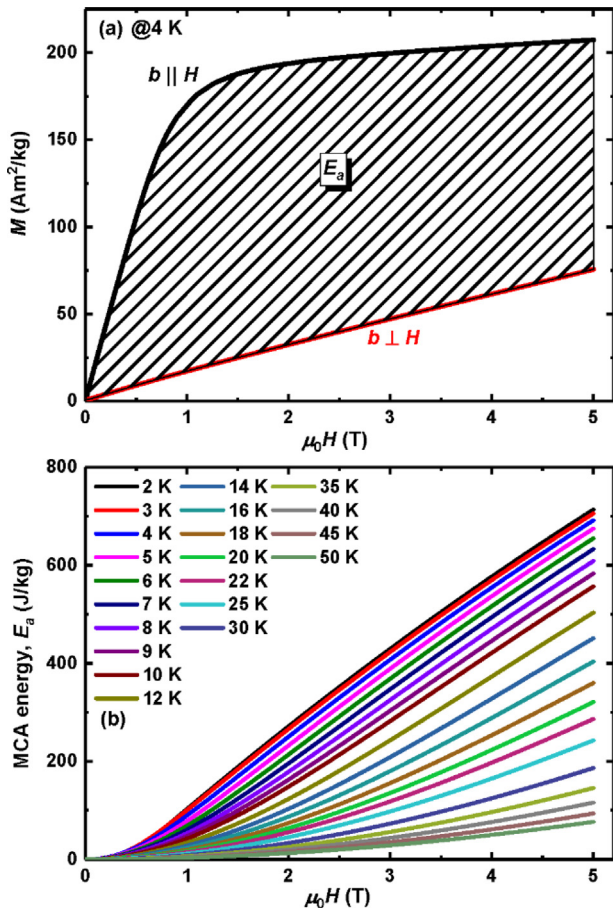
Fig. 8. (a) M-H curves at 4 K along the parallel and perpendicular directions, respectively. The E_a is denoted as the shaded area. (b) The field dependence of E_a at different temperatures.

Fig. 9. The (a) ΔS_R and (b) ΔT_R between the parallel and perpendicular directions as a function of temperature and magnetic field.

magnetization axis, θ is the angle between the magnetic field and easy magnetization axis, and α is the angle between the magnetization vector and easy magnetization axis, respectively. The MCA constants can be obtained by fitting the H-M curves along hard magnetization axis as follows:

$$H = \frac{2K_1}{M_S^2}M + \frac{4K_2}{M_S^4}M^3 \qquad (5)$$

Fig. 11(a) shows the H-M curve and the fitting data at 7 K along perpendicular direction as an example. The K_1 and K_2 values at 7 K are fitted to be 1574 and 717 J/kg, respectively. By putting K_1 and K_2 values into Eq. (4), the α can be estimated by minimizing E under certain magnetic field and θ. Then, the theoretical magnetization at different θ angle can be calculated by $M_{cal} = M_S \times \cos(\theta - \alpha)$. Fig. 11(b) shows the M_{cal} as a function of θ at 7 K in comparison with the experimental M_{exp} values at 0° and 90°. The M_{cal} is very close to the M_{exp} value, implying the validity of above theoretical calculation. Furthermore, the contribution of MCA to RMCE under adiabatic magnetization can be calculated by the following equation:

$$\Delta S_R(H, \theta, K_1) = \int_{90°}^{\theta} \frac{dE_K(H, \theta, K_1)}{T}$$
$$= K_1 \times \frac{\sin^2\alpha(H, \theta) - \sin^2\alpha(H, 90°)}{T} \qquad (6)$$

Fig. 11(c) shows the calculated $-\Delta S_R$ under 5 T at 7.5 K (just below the ΔS_R peak) and 15 K (just above the ΔS_R peak) as a function of rotation angle with the hard axis (perpendicular direction) as the starting direction. The $-\Delta S_R$ increases gradually with rotating the sample from hard axis to easy axis, and reaches the maximum value
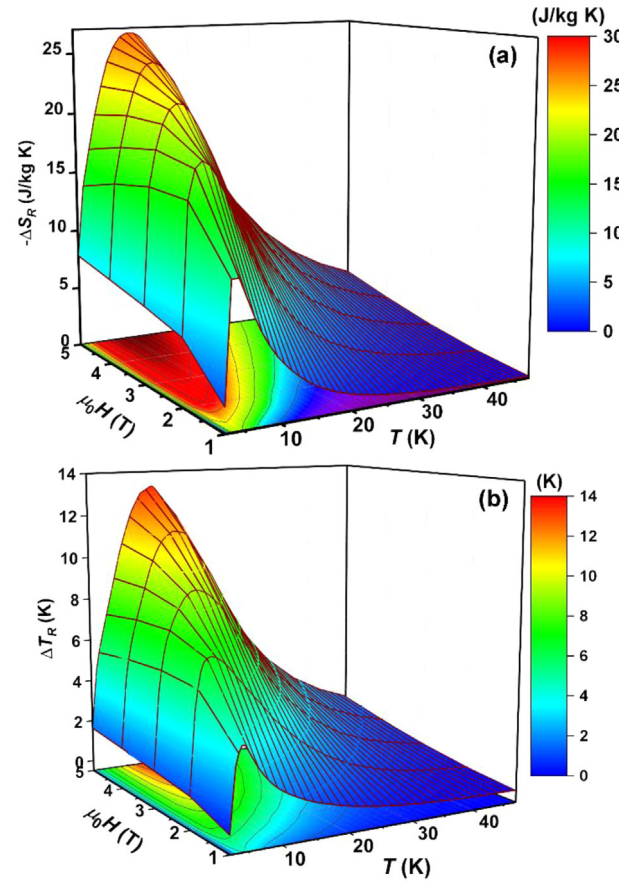
by rotating 90° and 270°. The maximum calculated $-\Delta S_R$ values are 21.5 and 10.3 J/kg K at 7.5 and 15 K, respectively. The corresponding experimental $-\Delta S_R$ values are 24.2 and 23.8 J/kg K at 7.5 and 15 K, respectively. The calculated value is very close to the experimental value below T_N, suggesting that the RMCE below T_N is mainly contributed by the MCA. On the contrary, the calculated value is much lower than the experimental value above T_N, revealing that the RMCE above T_N originates not only from MCA but also from other contributions, such as thermal fluctuations and spin flop process [19,20].

Fig. 12 compares the (a) $|\Delta S_R|$ and (b) ΔT_R of the textured HoNiSi with those of all other RMCE materials reported so far. The RMCE of textured HoNiSi is larger than those of most RMCE materials. Especially, the maximum $|\Delta S_R|$ of 26.7 J/kg K under 5 T for textured HoNiSi is the largest ΔS_R among all the RMCE materials. Moreover, the textured HoNiSi exhibits almost the highest RMCE covering a wide temperature range from 2 K to 40 K. Particularly, the RMCE under 2 T is even larger than those of most RMCE materials under high field of 5 T, such as $HoMnO_3$ (#3) [40], $TmMnO_3$ (#5) [20], and $ErGa_2$ (#21) [41]. This giant RMCE is related to the strongly coherent orientation of crystallographic texture and rare-earth Ho^{3+} ion moments in the textured HoNiSi. In addition, it is interesting to note that the MCE peak shifts remarkably towards higher temperature with increasing field. This is due to the different behavior of field-induced metamagnetic transition along different directions. The presence of field-induced FM correlation in PM region shifts the ΔS peak towards higher temperature along the parallel direction, while the ΔS peak remains constantly along the perpendicular direction due to the difficulty of field-induced metamagnetic transition (Figs. 7(e) and 7(f)), thus leading to the shift of ΔS_R peak towards higher temperature. Meanwhile, this broadening of ΔS_R peak also expands the working temperature range. Consequently, this giant RMCE of textured HoNiSi
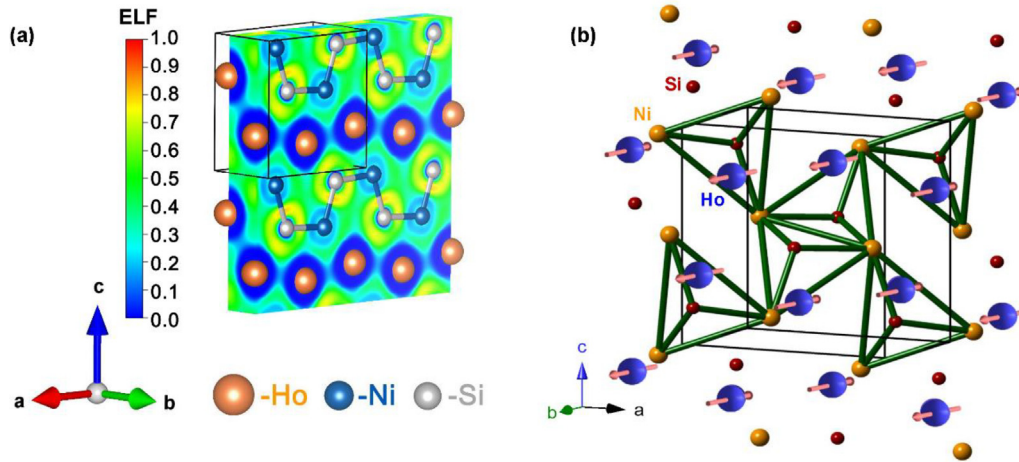
Fig. 10. (a) The distribution of ELF values within the 3D unit cell space (b) The perspective view of the TiNiSi-type crystal strucure of HoNiSi.
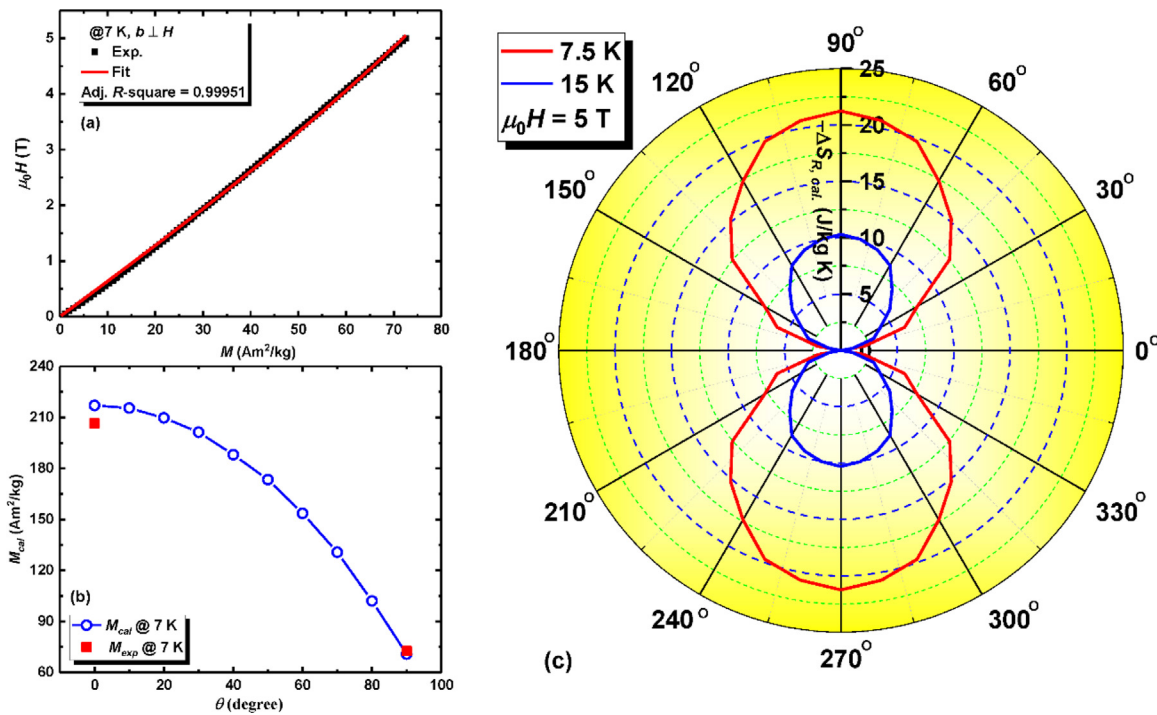

Fig. 11. (a) H-M curve and the fitting data at 7 K along the perpendicular direction. (b) The M_{cal} as a function of θ at 7 K in comparison with the experimental M_{exp} values at 0° and 90°. (c) The calculated $-\Delta S_R$ under 5 T at 7.5 K (just below the ΔS_R peak) and 15 K (just above the ΔS_R peak) as a function of rotation angle with the hard axis (perpendicular direction) as the starting direction.

over a wide temperature range especially under low magnetic field is desirable for the practical application of rotary magnetic refrigerator simply using permanent magnet.

5. Conclusions

In summary, coherent orientation of crystallographic texture and rare-earth ion moments has been found in textured HoNiSi polycrystal, which gives rise to the high anisotropy of magnetic and magnetocaloric properties. In addition to the AFM-FM transition at T_N, another anomaly is observed around T_1 just above T_N due to the presence of short-range FM ordering in PM state. A giant MCE is obtained along the easy magnetization axis while a low MCE is found along the hard magnetization axis. This large

anisotropic MCE results in a giant RMCE in textured HoNiSi. The magnetic anisotropy of HoNiSi is explained by the single-ion magnetic anisotropy theory, which originates from the synergy effect of CEF and spin-orbit coupling. Based on the CR model, the RMCE below T_N is mainly contributed by the MCA. In contrast, the RMCE above T_N originates not only from MCA but also from other contributions. To our knowledge, this is the largest ΔS_R among all the RMCE materials reported so far. Therefore, the giant RMCE especially under low magnetic field, wide working temperature range, and easy fabrication process make textured HoNiSi highly attractive candidate for low temperature RMCE materials. More importantly, this work demonstrates that the strongly coherent orientation of crystallographic texture and rare-earth ion moments is crucial to realize the large RMCE in polycrystalline materials.
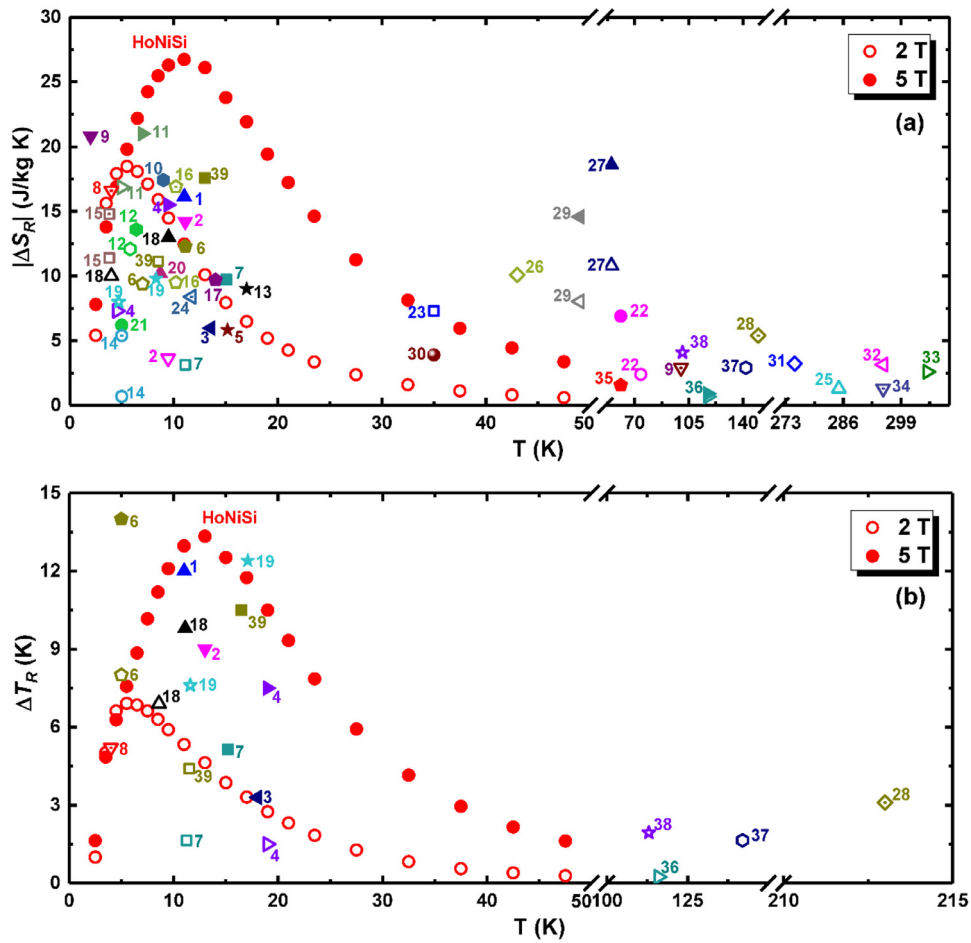
Fig. 12. The (a) $|\Delta S_R|$ and (b) ΔT_R of textured HoNiSi in comparison with the peak $|\Delta S_R|$ and ΔT_R values of other RMCE materials reported so far. Except the open symbols with a dot which will be specially indicated as follows, the open and solid symbols indicate the ΔS_R under 2 T and 5 T, respectively. The legend of these materials is listed as follows:

1- TbMnO$_3$ single crystal [42]	11- DyFeO$_3$ single crystal [43]	21-ErGa$_2$ single crystal [41]	31-NdCo$_5$ polycrystal [44]
2- DyMnO$_3$ single crystal [45]	12- ErFeO$_3$ single crystal [46]	22-TbAl$_2$ single crystal [47]	32- NdCo$_{4.8}$Si$_{0.2}$ polycrystal [44]
3- HoMnO$_3$ single crystal [40]	13- TmFeO$_3$ single crystal [48]	23-DyAl$_2$ single crystal [47]	33- NdCo$_{4.6}$Si$_{0.4}$ polycrystal [44]
4- ErMnO$_3$ single crystal [19]	14- TbCrO$_3$ single crystal, 4.5 T [49]	24- TmB$_4$ single crystal, 4.6 T [50]	34-NdCo$_4$Al polycrystal, 1 T [51]
5- TmMnO$_3$ single crystal [20]	15- DyCrO$_3$ single crystal, 4.5 T [49]	25- AlFe$_2$B$_2$ single crystal [52]	35-CrI$_3$ single crystal [53]
6- TbMn$_2$O$_5$ single crystal [54]	16- ErCrO$_3$ single crystal, 4.5 T [49]	26-NdGa single crystal [55]	36-Fe$_7$Se$_8$ single crystal [56]
7- HoMn$_2$O$_5$ single crystal [57]	17- ErAlO$_3$ single crystal [58]	27-PrSi single crystal [59]	37-Tb$_3$NiGe$_2$ polycrystal [60]
8- Gd$_2$CoMnO$_6$ single crystal, 9 T [61]	18- KEr(MoO$_4$)$_2$ single crystal [62]	28-Tb$_{0.2}$Gd$_{0.8}$ single crystal, 14 T [63]	38-Ho$_2$GdAl$_2$ polycrystal [35]
9- Tb$_2$CoMnO$_6$ single crystal, 7 T [64]	19-KTm(MoO$_4$)$_2$ single crystal [65]	29-TbNiAl single crystal [66]	39-DyNiSi polycrystal [21]
10- TbFeO$_3$ single crystal [48]	20-HoGa$_2$ single crystal [41]	30-HoAlGa polycrystal [67]	

Competing Declaration of Interest

The authors declare that they have no known competing financial interests or personal relationships that could have appeared to influence the work reported in this paper.

Acknowledgements

References

[1] A. Kitanovski, J. Tušek, U. Tomc, U. Plaznik, M. Ožbolt, A. Poredoš, Magnetocaloric Energy conversion: from Theory to Applications, Springer International Publishing, 2015.

[2] V. Franco, J.S. Blázquez, B. Ingale, A. Conde, The magnetocaloric effect and magnetic refrigeration near room temperature: materials and models, Annu. Rev. Mater. Res. 42 (2012) 305–342.

[3] O. Tegus, E. Brück, K.H.J. Buschow, F.R. de Boer, Transition-metal-based magnetic refrigerants for room-temperature applications, Nature 415 (2002) 150–152.

[4] V. Provenzano, A.J. Shapiro, R.D. Shull, Reduction of hysteresis losses in the magnetic refrigerant Gd$_5$Ge$_2$Si$_2$ by the addition iron, Nature 429 (2004) 853–857.

[5] J. Liu, T. Gottschall, K.P. Skokov, J.D. Moore, O. Gutfleisch, Giant magnetocaloric effect driven by structural transitions, Nat. Mater. 11 (2012) 620–626.

[6] V.K. Pecharsky, K.A. Gschneidner Jr., Giant magnetocaloric effect in Gd$_5$(Si$_2$Ge$_2$), Phys. Rev. Lett. 78 (1997) 4494–4497.

[7] T. Krenke, E. Duman, M. Acet, E.F. Wassermann, X. Moya, L. Mañosa, A. Planes, Inverse magnetocaloric effect in ferromagnetic Ni-Mn-Sn alloys, Nat. Mater. 4 (2005) 450–454.

[8] E.K. Liu, W.H. Wang, L. Feng, W. Zhu, G.J. Li, J.L. Chen, H.W. Zhang, G.H. Wu, C.B. Jiang, H.B. Xu, F. de Boer, Stable magnetostructural coupling with tunable magnetoresponsive effects in hexagonal ferromagnets, Nat. Commun. 3 (2012) 873.

[9] X. Moya, L.E. Hueso, F. Maccherozzi, A.I. Tovstolytkin, D.I. Podyalovskii, C. Ducati, L.C. Phillips, M. Ghidini, O. Hovorka, A. Berger, M.E. Vickers, E. Defay, S.S. Dhesi,

N.D. Mathur, Giant and reversible extrinsic magnetocaloric effects in La$_{0.7}$Ca$_{0.3}$MnO$_3$ films due to strain, Nat. Mater. 12 (2013) 52–58.

[10] B.G. Shen, J.R. Sun, F.X. Hu, H.W. Zhang, Z.H. Cheng, Recent progress in exploring magnetocaloric materials, Adv. Mater. 21 (2009) 4545–4564.

[11] F. Guillou, A.K. Pathak, D. Paudyal, Y. Mudryk, F. Wilhelm, A. Rogalev, V.K. Pecharsky, Non-hysteretic first-order phase transition with large latent heat and giant low-field magnetocaloric effect, Nat. Commun. 9 (2018) 2925.

[12] H. Zhang, Y.J. Sun, E. Niu, L.H. Yang, J. Shen, F.X. Hu, J.R. Sun, B.G. Shen, Large magnetocaloric effects of RFeSi (R = Tb and Dy) compounds for magnetic refrigeration in nitrogen and natural gas liquefaction, Appl. Phys. Lett. 103 (2013) 202412.

[13] S. Gupta, K.G. Suresh, Review on magnetic and related properties of RTX compounds, J. Alloys Compd. 618 (2015) 562–606.

[14] J.Y. Law, V. Franco, L.M. Moreno-Ramírez, A. Conde, D.Y. Karpenkov, I. Radulov, K.P. Skokov, O. Gutfleisch, A quantitative criterion for determining the order of magnetic phase transitions using the magnetocaloric effect, Nat. Commun. 9 (2018) 2680.

[15] X. Moya, S. Kar-Narayan, N.D. Mathur, Caloric materials near ferroic phase transitions, Nat. Mater. 13 (2014) 439–450.

[16] S.A. Nikitin, K.P. Skokov, Yu.S. Koshkid'ko, Yu.G. Pastushenkov, T.I. Ivanova, Giant rotating magnetocaloric effect in the region of spin-reorientation transition in the NdCo$_5$ single crystal, Phys. Rev. Lett. 105 (2010) 137205.

[17] M. Balli, S. Jandl, P. Fournier, A. Kedous-Lebouc, Advanced materials for magnetic cooling: fundamentals and practical aspects, Appl. Phys. Rev. 4 (2017) 021305.

[18] H. Zhang, B.G. Shen, Z.Y. Xu, J. Shen, F.X. Hu, J.R. Sun, Y. Long, Large reversible magnetocaloric effects in ErFeSi compound under low magnetic field change around liquid hydrogen temperature, Appl. Phys. Lett. 102 (2013) 092401.

[19] M. Balli, S. Jandl, P. Fournier, J. Vermette, D.Z. Dimitrov, Unusual rotating magnetocaloric effect in the hexagonal ErMnO$_3$ single crystal, Phys. Rev. B 98 (2018) 184414.

[20] J.L. Jin, X.Q. Zhang, H. Ge, Z.H. Cheng, Rotating field entropy change in hexagonal TmMnO$_3$ single crystal with anisotropy paramagnetic response, Phys. Rev. B 85 (2012) 214426.

[21] H. Zhang, Y.W. Li, E.K. Liu, Y.J. Ke, J.L. Jin, Y. Long, B.G. Shen, Giant rotating magnetocaloric effect induced by highly texturing in polycrystalline DyNiSi compound, Sci. Rep. 5 (2015) 11929.

[22] X.Q. Zheng, H. Wu, J. Chen, B. Zhang, Y.Q. Li, F.X. Hu, J.R. Sun, Q.Z. Huang, B.G. Shen, The physical mechanism of magnetic field controlled magnetocaloric effect and magnetoresistance in bulk PrGa compound, Sci. Rep. 5 (2015) 14970.

[23] G. Chen, H.Z. Fu, Novel Metal Materials With Non-Equilibrium Solidification (In Chinese), Science Press Publishing, Beijing, 2004.

[24] Y. Ouyang, M.X. Zhang, J. Li, A.R. Yan, J. Liu, A high-throughput study of magnetocaloric materials: gradient solidification applied to La-Fe-Si, Intermetallics 108 (2019) 100–108.

[25] B.A. Hunter, A visual Rietveld program, international union of crystallography commission on powder diffraction, Newsletter 20 (1998) 21.

[26] D.X. Chen, E. Pardo, A. Sanchez, Demagnetizing factors of rectangular prisms and ellipsoids, IEEE Trans. Magn. 38 (2002) 1742–1752.

[27] V. Yannello, F. Guillou, A.A. Yaroslavtsev, Z.P. Tener, F. Wilhelm, A.N. Yaresko, S.L. Molodtsov, A. Scherz, A. Rogalev, M. Shatruk, Revisiting bond breaking and making in EuCo$_2$P$_2$: where are the electrons? Chem. Eur. J. 25 (2019) 5865–5869.

[28] A. Szytula, M. Balanda, M. Hofmann, J. Leciejewicz, M. Kolenda, B. Penc, A. Zygmunt, Antiferromagnetic properites of ternary silicides RNiSi (R = Tb–Er), J. Magn. Magn. Mater. 191 (1999) 122–132.

[29] H. Zhang, Y.Y. Wu, Y. Long, H.S. Wang, K.X. Zhong, F.X. Hu, J.R. Sun, B.G. Shen, Large reversible magnetocaloric effect in antiferromagnetic HoNiSi compound, J. Appl. Phys. 116 (2014) 213902.

[30] F. Yuan, J. Du, B.L. Shen, Controllable spin-glass behavior and large magnetocaloric effect in Gd-Ni-Al bulk metallic glasses, Appl. Phys. Lett. 101 (2012) 032405.

[31] N.K. Singh, V.K. Pecharsky, K.A. Gschneidner Jr, Unusual magnetic properties of (Er$_{1-x}$Gd$_x$)$_5$Si$_4$ compounds, Phys. Rev. B 77 (2008) 054414.

[32] J.L. Wang, C. Marquina, M.R. Ibarra, G.H. Wu, Structure and magnetic properties of RNi$_2$Mn compounds, Phys. Rev. B 73 (2006) 094436.

[33] Z.W. Ouyang, V.K. Pecharsky, K.A. Gschneidner Jr., D.L. Schlagel, T.A. Lograsso, Short-range anisotropic ferromagnetic correlations in the paramagnetic and antiferromagnetic phases of Gd$_5$Ge$_4$, Phys. Rev. B 74 (2006) 094404.

[34] P. Arora, M.K. Chattopadhyay, S.B. Roy, Magnetic properties and large magnetocaloric effect of DyPt$_2$, J. Appl. Phys. 106 (2009) 093912.

[35] M.L. Wu, H. Zhang, K.W. Long, K. Tao, Y.X. Wang, C.F. Xing, Y.N. Xiao, L.C. Wang, Y. Long, Magnetocaloric effect in textured polycrystalline Ho$_2$GdAl$_2$, Mater. Lett. 205 (2017) 40–43.

[36] M. Fries, K.P. Skokov, D.Y. Karpenkov, V. Franco, S. Ener, O. Gutfleisch, The influence of magnetocrystalline anisotropy on the magnetocaloric effect: a case study on Co$_2$B, Appl. Phys. Lett. 109 (2016) 232406.

[37] W.P. Wolf, Effect of crystalline electric fields on ferromagnetic anisotropy, Phys. Rev. 108 (1957) 1152–1157.

[38] M.I. Darby, E.D. Isaac, Magnetocrystalline anisotropy of ferro- and ferrimagnetics, IEEE Trans. Magn. 10 (1974) 259–304.

[39] J.L. Jin, X.Q. Zhang, G.K. Li, Z.H. Cheng, L. Zheng, Y. Lu, Giant anisotropy of magnetocaloric effect in TbMnO$_3$ single crystals, Phys. Rev. B 83 (2011) 184431.

[40] M. Balli, B. Roberge, J. Vermette, S. Jandl, P. Fournier, M.M. Gospodinov, Magnetocaloric properties of the hexagonal HoMnO$_3$ single crystal revisited, Phys. Conden. Matter 478 (2015) 77–83.

[41] R.D. dos Reis, L.M. da Silva, A.O. dos Santos, A.M.N Medina, L.P. Cardoso, F.C.G. Gandra, Anisotropic magnetocaloric effect in ErGa$_2$ and HoGa$_2$ single-crystals, J. Alloys Compd. 582 (2014) 461–465.

[42] M. Balli, P. Fournier, S. Jandl, S. Mansouri, A. Mukhin, Y.V. Ivanov, A.M. Balbashov, Comment on "Giant anisotropy of magnetocaloric effect in TbMnO$_3$ single crystals", Phys. Rev. B 96 (2017) 146401.

[43] Y.J. Ke, X.Q. Zhang, H. Ge, Y. Ma, Z.H. Cheng, Low field induced giant anisotropic magnetocaloric effect in DyFeO$_3$ single crystal, Chin. Phys. B 24 (2015) 37501.

[44] K. Wang, M.X. Zhang, J. Liu, H.B. Luo, J. Sun, Crystal structure, spin reorientation, and rotating magnetocaloric properties of NdCo$_{5-x}$Si$_x$ compounds, J. Appl. Phys. 125 (2019) 243901.

[45] M. Balli, S. Mansouri, S. Jandl, P. Fournier, D.Z. Dimitrov, Large rotating magnetocaloric effect in the orthorhombic DyMnO$_3$ single crystal, Solid State Commun. 239 (2016) 9–13.

[46] R.X. Huang, S.X. Cao, W. Ren, S. Zhan, B.J. Kang, J.C. Zhang, Large rotating field entropy change in ErFeO$_3$ single crystal with angular distribution ocntribution, Appl. Phys. Lett. 103 (2013) 162412.

[47] J.C.B. Monteiro, F.G. Gandra, Direct measurements of conventional and anisotropic magnetocaloric effect in binary RAl$_2$ single crystals, J. Appl. Phys. 121 (2017) 213904.

[48] Y.J. Ke, X.Q. Zhang, Y. Ma, Z.H. Cheng, Anisotropic magnetic entropy change in RFeO$_3$ single crystals (R = Tb, Tm, or Y), Sci. Rep. 6 (2016) 19775.

[49] L.H. Yin, J. Yang, P. Tong, X. Luo, C.B. Park, K.W. Shin, W.H. Song, J.M. Dai, K.H. Kim, X.B. Zhu, Y.P. Sun, Role of rare earth in the magnetic, magnetocaloric and magnetoelectric properties of RCrO$_3$ (R = Dy, Nd, Tb, Er) crystals, J. Mater. Chem. C 4 (2016) 11198–11204.

[50] M. Orendáč, S. Gabáni, E. Gažo, G. Pristáš, N. Shitsevalova, K. Siemensmeyer, K. Flachbart, Rotating magnetocaloric effect in TmB$_4$ - A comparison between estimations based on heat capacity and magnetization measurements, J. Magn. Magn. Mater. 482 (2019) 186–191.

[51] Y. Hu, Q.B. Hu, C.C. Wang, Q.Q. Cao, W.L. Gao, D.H. Wang, Y.W. Du, Large room-temperature rotating magnetocaloric effect in NdCo$_4$Al polycrystalline alloy, Solid State Commun. 250 (2017) 45–48.

[52] R. Barua, B.T. Lejeune, L. Ke, G. Hadjipanayis, E.M. Levin, R.W. McCallum, M.J. Kramer, L.H. Lewis, Anisotropic magnetocaloric response in AlFe$_2$B$_2$, J. Alloys Compd. 745 (2018) 505–512.

[53] Y. Liu, C. Petrovic, Anisotropic magnetocaloric effect in single crystals of CrI$_3$, Phys. Rev. B 97 (2018) 174418.

[54] M. Balli, S. Jandl, P. Fournier, D.Z. Dimitrov, Giant rotating magnetocaloric effect at low magnetic fields in multiferroic TbMn$_2$O$_5$ single crystals, Appl. Phys. Lett. 108 (2016) 102401.

[55] Y.S. Jia, T. Namiki, S. Kasai, L.W. Li, K. Nishimura, Magnetic anisotropy and large low field rotating magnetocaloric effect in NdGa single crystal, J. Alloys Compd. 757 (2018) 44–48.

[56] I. Radelytskyi, P. Aleshkevych, D.J. Gawryluk, M. Berkowski, T. Zajarniuk, A. Szewczyk, M. Gutowska, L. Hawelek, P. Wlodarczyk, J. Fink-Finowicki, R. Minikayev, R. Diduszko, Y. Konopelnyk, M. Kozlowski, R. Puzniak, H. Szymczak, Structural, magnetic, and magnetocaloric properties of Fe7Se8 single crystals, J. Appl. Phys. 124 (2018) 143902.

[57] M. Balli, S. Jandl, P. Fournier, M.M. Gospodinov, Anisotropy-enhanced giant reversible rotating magnetocaloric effect in HoMn$_2$O$_5$ single crystals, Appl. Phys. Lett. 104 (2014) 232402.

[58] X.Q. Zhang, Y.D. Wu, Y. Ma, Q.Y. Dong, Y.J. Ke, Z.H. Cheng, Large rotating magnetocaloric effect in ErAlO$_3$ single crystal, AIP Adv. 7 (2017) 056418.

[59] P.K. Das, A. Bhattacharyya, R. Kulkarni, S.K. Dhar, A. Thamizhavel, Anisotropic magnetic properties and giant magnetocaloric effect of single-crystal PrSi, Phys. Rev. B 89 (2014) 134418.

[60] Y.X. Wang, H. Zhang, K.W. Long, C.F. Xing, Y.N. Xiao, L.Q. Su, L.C. Wang, Y. Long, Rotating magnetocaloric effect in textured polycrystalline Tb$_3$NiGe$_2$ compound with successive magnetic transitions, Intermetallics 100 (2018) 175–180.

[61] J.Y. Moon, M.K. Kim, Y.J. Choi, N. Lee, Giant anisotropic magnetocaloric effect in double-perovskite Gd$_2$CoMnO$_6$ single crystals, Sci. Rep. 7 (2017) 16099.

[62] V. Tkáč, A. Orendáčová, E. Čižmár, M. Orendáč, A. Feher, A.G. Anders, Giant reversible rotating cryomagnetocaloric effect in KEr(MoO$_4$)$_2$ induced by a crystal-field anisotropy, Phys. Rev. B 92 (2015) 024406.

[63] S.A. Nikitin, T.I. Ivanova, A.I. Zvonov, Y.S. Koshkid'ko, J. Ćwik, K. Rogacki, Magnetization, magnetic anisotropy and magnetocaloric effect of the Tb$_{0.2}$Gd$_{0.8}$ single crystal in high magnetic fields up to 14 T in region of a phase transition, Acta Mater. 161 (2018) 331–337.

[64] J.Y. Moon, M.K. Kim, D.G. Oh, J.H. Kim, H.J. Shin, Y.J. Choi, N. Lee, Anisotropic magnetic properties and giant rotating magnetocaloric effect in double-perovskite Tb$_2$CoMnO$_6$, Phys. Rev. B 98 (2018) 174424.

[65] R. Tarasenko, V. Tkáč, A. Orendáčová, M. Orendáč, A. Feher, Experimental study of the rotational magnetocaloric effect in KTm(MoO$_4$)$_2$, Phys. B Conden. Matter. 538 (2018) 116–119.

[66] J. Kaštil, P. Javorský, J. Pospíšil, Anisotropic magnetocaloric effect in TbNiAl, J. Alloys Compd. 509 (2011) 5931–5934.

[67] Y. Zhang, X.Q. Zheng, J.F. Xiong, S.L. Zuo, Q.Y. Dong, T.Y. Zhao, B.G. Shen, Anisotropic magnetocaloric effect in HoAlGa polycrystalline compound, AIP Adv. 8 (2018) 056427.